

## Article

# Electrical Resistivity and Phase Evolution of Fe–N Binary System at High Pressure and High Temperature

Yunzhe Wang<sup>1</sup>, Fan Yang<sup>1</sup>, Chunhua Shen<sup>2</sup>, Jing Yang<sup>3</sup> , Xiaojun Hu<sup>1,\*</sup>  and Yingwei Fei<sup>3,\*</sup>

<sup>1</sup> School of Science, Wuhan University of Technology, Wuhan 430070, China; wzhwang@whut.edu.cn (Y.W.); fyang@whut.edu.cn (F.Y.)

<sup>2</sup> Center for Materials Research and Analysis, Wuhan University of Technology, Wuhan 430070, China; chunhuashen@whut.edu.cn

<sup>3</sup> Earth and Planets Laboratory, Carnegie Institution for Science, Washington, DC 20015, USA; jyang@carnegiescience.edu

\* Correspondence: xjhu@whut.edu.cn (X.H.); yfei@carnegiescience.edu (Y.F.)

**Abstract:** Partitioning experiments and the chemistry of iron meteorites indicate that the light element nitrogen could be sequestered into the metallic core of rocky planets during core–mantle differentiation. The thermal conductivity and the mineralogy of the Fe–N system under core conditions could therefore influence the planetary cooling, core crystallization, and evolution of the intrinsic magnetic field of rocky planets. Limited experiments have been conducted to study the thermal properties and phase relations of Fe–N components under planetary core conditions, such as those found in the Moon, Mercury, and Ganymede. In this study, we report results from high-pressure experiments involving electrical resistivity measurements of Fe–N phases at a pressure of 5 GPa and temperatures up to 1400 K. Four Fe–N compositions, including Fe–10%N, Fe–6.4%N, Fe–2%N, and Fe–1%N (by weight percent), were prepared and subjected to recovery experiments at 5 GPa and 1273 K. These experiments show that Fe–10%N and Fe–6.4%N form a single hexagonal close-packed phase ( $\epsilon$ -nitrides), while Fe–2%N and Fe–1%N exhibit a face-centered cubic structure ( $\gamma$ -Fe). In separate experiments, the resistivity data were collected during the cooling after compressing the starting materials to 5 GPa and heating to  $\sim$ 1400 K. The resistivity of all compositions, similar to the pure  $\gamma$ -Fe, exhibits weak temperature dependence. We found that N has a strong effect on the resistivity of metallic Fe under rocky planetary core conditions compared to other potential light elements such as Si. The temperature-dependence of the resistivity also revealed high-pressure phase transition points in the Fe–N system. A congruent reaction,  $\epsilon \rightleftharpoons \gamma'$ , occurs at  $\sim$ 673 K in Fe–6.4%N, which is  $\sim$ 280 K lower than that at ambient pressure. Furthermore, the resistivity data provided constraints on the high-pressure phase boundary of the polymorphic transition,  $\gamma \rightleftharpoons \alpha$ , and an eutectoid equilibrium of  $\gamma' \rightleftharpoons \alpha + \epsilon$ . The data, along with the recently reported phase equilibrium experiments at high pressures, enable construction of a phase diagram of the Fe–N binary system at 5 GPa.



**Citation:** Wang, Y.; Yang, F.; Shen, C.; Yang, J.; Hu, X.; Fei, Y. Electrical Resistivity and Phase Evolution of Fe–N Binary System at High Pressure and High Temperature. *Minerals* **2024**, *14*, 467. <https://doi.org/10.3390/min14050467>

Academic Editor: Yoichi Nakajima

Received: 2 April 2024

Revised: 23 April 2024

Accepted: 27 April 2024

Published: 28 April 2024

**Keywords:** iron nitrides; high pressure; electrical resistivity; phase transition; terrestrial planets



**Copyright:** © 2024 by the authors. Licensee MDPI, Basel, Switzerland. This article is an open access article distributed under the terms and conditions of the Creative Commons Attribution (CC BY) license (<https://creativecommons.org/licenses/by/4.0/>).

## 1. Introduction

The intrinsic magnetic fields observed on Earth and terrestrial planets are thought to originate from the convection processes within their metallic liquid cores [1–3]. This convection could be driven by thermal or chemical buoyancy depending on the thermal conductivity of the core minerals and the temperature gradient across the core–mantle boundary. The thermal transport properties of the core minerals are thus crucial for understanding planetary cooling, core dynamics, and the histories of the magnetic fields of terrestrial planets. However, direct measurements of the thermal conductivity of minerals under the conditions relevant to planetary cores remain challenging [4]. A more readily

available alternative is to measure the electrical resistivity, which can be converted to thermal conductivity by the Wiedemann–Franz law for metallic materials.

Given that Earth’s core and terrestrial planetary cores are mainly composed of iron (Fe) alloyed with nickel (Ni) and some light elements, such as silicon (Si), sulfur (S), oxygen (O), carbon (C), and hydrogen (H) [5,6], numerous high-pressure experiments have been conducted to measure the electrical resistivity of Fe [7–16] and Fe alloys in Fe–Si [17–26], Fe–S [27–32], Fe–P [33,34], and Fe–C [35] systems. The experimental results, along with computational studies [36–45], have constituted the primary source of resistivity data used in modeling the thermal evolution of planetary interiors.

Nitrogen (N), the fifth most abundant element in the solar system, is prevalent on the Earth’s surface as the main component of the atmosphere and a vital nutrient for life. It is, however, not conventionally considered as a potential light element in the planetary core due to its high volatility at atmospheric pressure and the lack of experimental constraints on its behavior during the planetary core–mantle differentiation. As demonstrated by metallurgical data, the solubility of N in liquid Fe at 1 atm is as low as  $\sim 0.045$  wt% and sharply decreases with increased temperatures and concentrations of solute Ni [46,47]. Early estimates of the chemical composition of bulk silicate Earth largely presumed that N was only abundant on the surface but depleted in the deep interior [48,49]. However, recent chemical analysis, combined with experimental data on N solubility in geological materials, has suggested that bulk silicate Earth (BSE) reserves  $\sim 7 \pm 4$  times the present atmospheric N ( $4 \times 10^{18}$  kg) through subduction processes, with the core containing  $\sim 10^{20}$  kg of N [50]. In addition, the discovery of exoplanets has opened a new dimension regarding the role of N in planetary interiors.

Despite its prevalence on the surface, N is relatively depleted in BSE compared to other major volatiles such as C [51,52], resulting in a higher C/N ratio ( $\sim 49.0 \pm 9.3$ ) [53] for BSE compared to primitive accretion blocks such as CI carbonaceous chondrites ( $\sim 17.0 \pm 3.0$ ) [54] and enstatite chondrites ( $\sim 13.7 \pm 12.1$ ) [55]. Superchondritic BSE has been directly linked to the highly volatile and/or siderophile character of N, i.e., large amounts of N have been either lost to the atmosphere through the degassing process [56–58] or sequestered into the planetary metallic core during the magma ocean crystallization [52,59]. Recent partitioning experiments [60–64] and stability studies of various Fe–N stoichiometries under conditions relevant to the planetary core [65–71] support the hypothesis that the planetary core is an appreciable reservoir for nitrogen. Additionally, the analysis of N-bearing components in meteorites suggests that N is moderately siderophilic [55]. The assertion of the appreciable N in planetary cores can also be made on the basis of meteorite chemistry. For example, the taenite phase in most iron meteorites can contain N approaching 1 wt%, the nitrides Carlsbergite (CrN) and Roaldite ((Fe,Ni)<sub>4</sub>N) frequently present in meteorites as characteristic minerals [72], and a new nitride Uakitite (VN) has been recently found in iron meteorites [73].

Similar to carbon, N alloying with Fe profoundly alters the allotropy of Fe through the formation of nitrides and solid solutions. Under ambient pressure, equilibrium Fe–N solid phases include solid solutions such as  $\alpha$ -Fe (bcc) and  $\gamma$ -Fe (fcc) and nitrides including  $\gamma'$ -Fe<sub>4</sub>N (fcc) with a narrow range of composition near 20 at.% N,  $\epsilon$ -Fe<sub>3</sub>N<sub>x</sub> (hcp) with  $0.66 < x < 1.47$ , and  $\xi$ -Fe<sub>2</sub>N (orthorhombic) with a composition ranging from about 33 at.% N to an unknown upper limit [74,75]. However, due to the lack of phase equilibrium data at high pressures, our understanding of the candidate N-bearing phase under conditions relevant to the Earth and terrestrial planetary interiors is primarily derived from the Fe–N phase diagram at atmospheric pressure [75] and limited high-pressure experiments which only focused on the study of the equation of state [66,68–71,76–78].

Controversy exists regarding the high-pressure stability of  $\gamma'$ -Fe<sub>4</sub>N. Earlier experiments suggested that  $\gamma'$ -Fe<sub>4</sub>N might transform to the  $\epsilon$  phase or undergo an order–disorder transition at  $\sim 17$ – $32$  GPa and 300 K [71,78]. However, recent experiments indicate no structural transformation of  $\gamma'$ -Fe<sub>4</sub>N up to 77 GPa at 300 K [66,68], consistent with the retention to 99 GPa at 300 K [70]. Despite the fact that the stability of  $\gamma'$ -Fe<sub>4</sub>N upon room-

temperature compression suggests that  $\gamma'$ -Fe<sub>4</sub>N is a potential N-bearing phase in planetary interiors [66,68,76], recovery experiments conducted by Wetzal et al. [79,80] at 2–13 GPa and up to 1273 K argued that  $\gamma'$ -Fe<sub>4</sub>N is a metastable phase and unlikely to occur in the Fe–N system at pressures exceeding 10 GPa.

In addition to the poor understanding of the core mineralogy of the Fe–N system, little is known about the effect of N on the transport property of Fe. Only one experiment has been performed to study the resistivity of Fe nitride at high pressure [76], revealing that nitride Fe<sub>2</sub>N behaves as a semiconductor with a resistivity value over 3000  $\Omega\text{m}$  up to 70 GPa and room temperature. It suggests that N would have enormous effect on the thermal conductivity of Fe and therefore the heat transport in the planetary core. However, the most recent computational studies suggest that the resistivity of the Fe–N system is comparable to other Fe alloys in the Fe–Si, Fe–C, Fe–O, Fe–S, Fe–H, and Fe–P systems [38]. Furthermore, recent experimental findings by Ma et al. [81] reported that the bulk Fe<sub>2</sub>N synthesized under high pressure conditions exhibits good metallic conductivity, with a resistivity of  $172 \times 10^{-8} \Omega\text{m}$  at ambient condition, similar to the experimental results for Fe alloys mentioned above.

In this study, we measured the electrical resistivity of four Fe–N compositions, including two solid solutions (Fe–1%N and Fe–2%N by weight percent) and two nitrides (containing 6.4%N and 10%N, respectively). Experiments were conducted at a pressure of 5 GPa and temperatures up to 1400 K using a cubic press combined with our recently developed high-pressure technique for resistivity measurement [82]. We discussed the effect of N on the resistivity of Fe based on the measured data. These data were also combined with recovery experiments to construct a phase diagram of the Fe–N system at high pressure that would help to understand the possible N-bearing phases in planetary cores.

## 2. Experiments

### 2.1. Starting Materials

We prepared two starting materials by nitriding Fe powder (99.95%, average 10  $\mu\text{m}$  particle, Alfa Aesar) with a NH<sub>3</sub>/H<sub>2</sub> gas mixture in a tube furnace at 750 K and 793 K, respectively. The yielded nitride powders showed 9.97 wt% N (denoted as Fe–10N) and 6.41 wt% N (Fe–6.4N), respectively. Two additional starting materials were prepared by mixing the synthesized Fe–6.4N powder with pure Fe, with nitrogen contents of 1 wt% (Fe–1N) and 2 wt% (Fe–2N), respectively.

### 2.2. Sample Characterization

The N content in the starting nitride powder was analyzed using the carrier gas hot extraction method using an NHO combined analyzer (ONH836, Leco, USA). The phase constituents in the starting nitride powders and recovered samples were characterized through the X-ray diffraction (XRD) technique (anode material: Co, K<sub>a1</sub>,  $\lambda = 1.78901 \text{ \AA}$ , Bruker D8 Advance diffractometer). Diffraction data was collected in the angular range from 30° to 140°. For the recovered samples, we scanned the surface toward the thermocouple junction. The diffraction data were analyzed with Rietveld refinements using Bruker's Topas 5 software. The analysis yielded phase constituents, lattice parameters, and the weight fraction of each phase in the sample.

### 2.3. Electrical Resistivity Measurements

The high-pressure experiments were conducted using a large-volume cubic press. A newly developed high-pressure technique was employed for measuring the electrical resistivity as illustrated in Figure 1 and described in [82]. This technique is on the basis of the Van der Pauw four-wire method and is known to provide reliable electrical resistivity measurements. Initially, the starting Fe–N powder was pre-pressed into a disk with a hard steel die at 20 MPa and assembled in the hBN tube. The electrode wires were positioned in contact with the disk on its periphery as shown in Figure 1c. A K-type thermocouple was separated from the sample by a 0.5 mm-thick hBN plate. The sample was first compressed

to 5 GPa at room temperature and then heated to  $\sim 1400$  K for at least 1 h. Data collection was performed while gradually decreasing the temperature. A typical uncertainty in the measured resistivity is  $\sim 2\%$ . The detailed information for sample assembly, data collection, and uncertainty analysis can be found in our recent work [82].

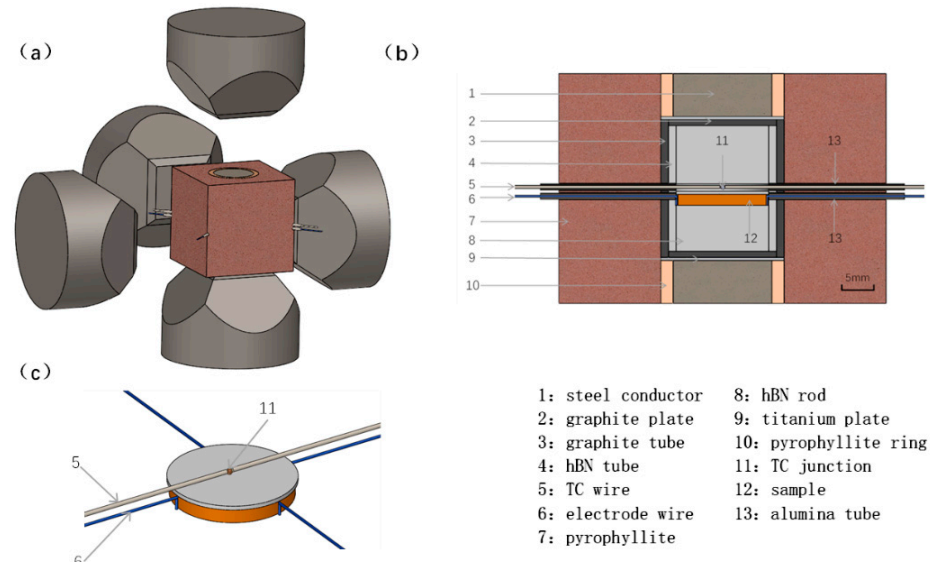


**Figure 1.** (a) Schematic diagram of the assemblage and large-volume press technique for electrical resistivity measurement at a high pressure and high temperature. (b) Cross-section view of the experimental configuration, showing the cell assembly with the sample, electrodes, and thermocouple. (c) Enlarged view to show the position of the thermocouple (TC) junction and the contact mode between the sample and electrodes.

#### 2.4. Recovery Experiments

In addition to the resistivity measurements, high-pressure recovery experiments were conducted for a better understanding of the stable phases of the Fe–N sample at 5 GPa and different temperatures. For the phase stability study, the Fe–N powder was firstly pre-pressed into a pellet and encapsulated using a tantalum container. The container was then assembled into an hBN tube in a manner very similar to the configuration shown in Figure 1b, with exception that no electrodes were involved. For each recovery experiment, we symmetrically assembled two samples into hBN tubes to sandwich the K-type thermocouple joint at the center. All samples were subjected to heat treatment at 5 GPa and 1273 K for 2 h and then quenched to room temperature by switching off the power. Upon decompression, the container was removed, and sample was polished into a pellet with a parallelism better than 0.01 mm for further phase characterization.

### 3. Results and Discussion

#### 3.1. N Content and Phase Identification of the Starting Materials

The measured nitrogen and oxygen composition of the starting materials are 9.97 (0.19) wt% N and 0.75 (0.13) wt% O for Fe–10N and 6.41(0.15) wt% N and 0.44(0.09) wt% O for Fe–6.4N. The presence of impurity O in both powders is attributed to oxygen introduction during the nitriding process. The diffraction data and Rietveld refinement results revealed that both powders consist of multiple phases (Figure 2). The Fe–10N comprises primarily  $\epsilon$ -Fe<sub>3</sub>N<sub>1.33</sub> (98.8 wt%) with minor  $\gamma'$ -Fe<sub>4</sub>N (1.2 wt%) and a trace amount of wüstite FeO<sub>x</sub>. The lattice parameters for those nitride phases are  $a = 4.7626(2)$  Å and  $c = 4.4105(1)$  Å for  $\epsilon$ -Fe<sub>3</sub>N<sub>1.33</sub> and  $a = 3.7957(2)$  Å for  $\gamma'$ -Fe<sub>4</sub>N. The average N content calculated from the Rietveld analysis is 9.957 wt%, in good agreement with the chemical analysis. For the Fe–6.4N, Rietveld refinement yielded 76.6 wt%  $\gamma'$ -Fe<sub>4</sub>N, 19.7%  $\epsilon$ -Fe<sub>3</sub>N<sub>1.33</sub>, and 3.7 wt%  $\alpha$ -Fe. The lattice parameters are  $a = 3.7953(2)$  Å for  $\gamma'$ -Fe<sub>4</sub>N,  $a = 4.7562(3)$  Å and  $c = 4.4069(2)$  Å

for  $\epsilon$ -Fe<sub>3</sub>N<sub>1.33</sub>, and  $a = 2.8636(2)$  Å for  $\alpha$ -Fe. The average N content calculated from the XRD analysis is 6.491 wt%, consistent with the result of chemical analysis.

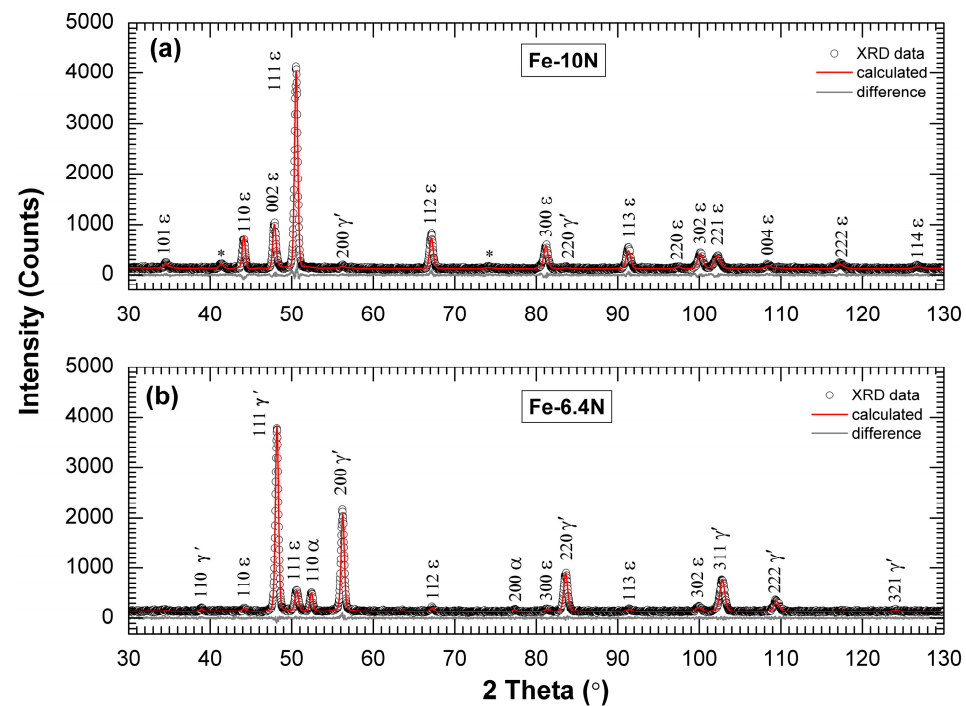


**Figure 2.** X-ray diffraction data of the synthesized samples showing  $\epsilon$ (a) or  $\gamma'$  (b) as the dominant nitride phase. The diffraction data, Rietveld refinement fits, and their difference are represented by black circles, red, and dark gray lines, respectively. Peaks of trace wüstite are marked with asterisks.

### 3.2. Phase Characterization of the Recovered Samples

We analyzed the diffraction data of the recovered samples. The results from analysis of the X-ray diffraction data are shown in Figure 3 and Table 1. Both Fe–10N and Fe–6.4N samples were transformed into a hexagonal close-packed (hcp) structure at 5 GPa and 1273 K. The transformation to a single phase for both compositions indicates that these compositions are in the stability field of the  $\epsilon$ -phase at 5 GPa and 1273 K, in agreement with a recent experimental study [79]. The diffraction peaks of Fe–10N shift toward lower angles compared to Fe–6.4N due to the relatively larger lattice parameters of Fe–10N. The lattice parameters are  $a = 4.7581(1)$  Å and  $c = 4.4066(1)$  Å for Fe–10N and  $a = 4.6286(2)$  Å and  $c = 4.3521(2)$  Å for Fe–6.4N (Table 1). The cell volume was calculated using the formula  $V = \frac{\sqrt{3}}{2}a^2c$  for the hcp structure, which was used to determine the N content in the nitride phase according to Liapina et al. 2004 [83], as in recent studies [79,80]. It was observed that both recovered samples contain slightly less nitrogen than the initial powders, with 9.56 wt% N and 5.86 wt% N in the recovered Fe–10N and Fe–6.4N samples, respectively, compared to 9.97 wt% N and 6.41 wt% N in the starting materials. Although recent recovery experiments showed no detectable N loss at 2–13 GPa and up to 1273 K [79,80], the slight N loss in this work is probably attributed to the temperature gradient in the large sample chamber. We further calculated the  $x$  value in the formula Fe<sub>3</sub>N <sub>$x$</sub>  based on the N content in the recovered  $\epsilon$ -phase, yielding 1.268 for Fe–10N and 0.747 for Fe–6.4N sample. These values are consistent with the established relationship between the unit cell volume of  $\epsilon$ -Fe<sub>3</sub>N <sub>$x$</sub>  and the N content under ambient conditions [69], as shown in Figure 3c.

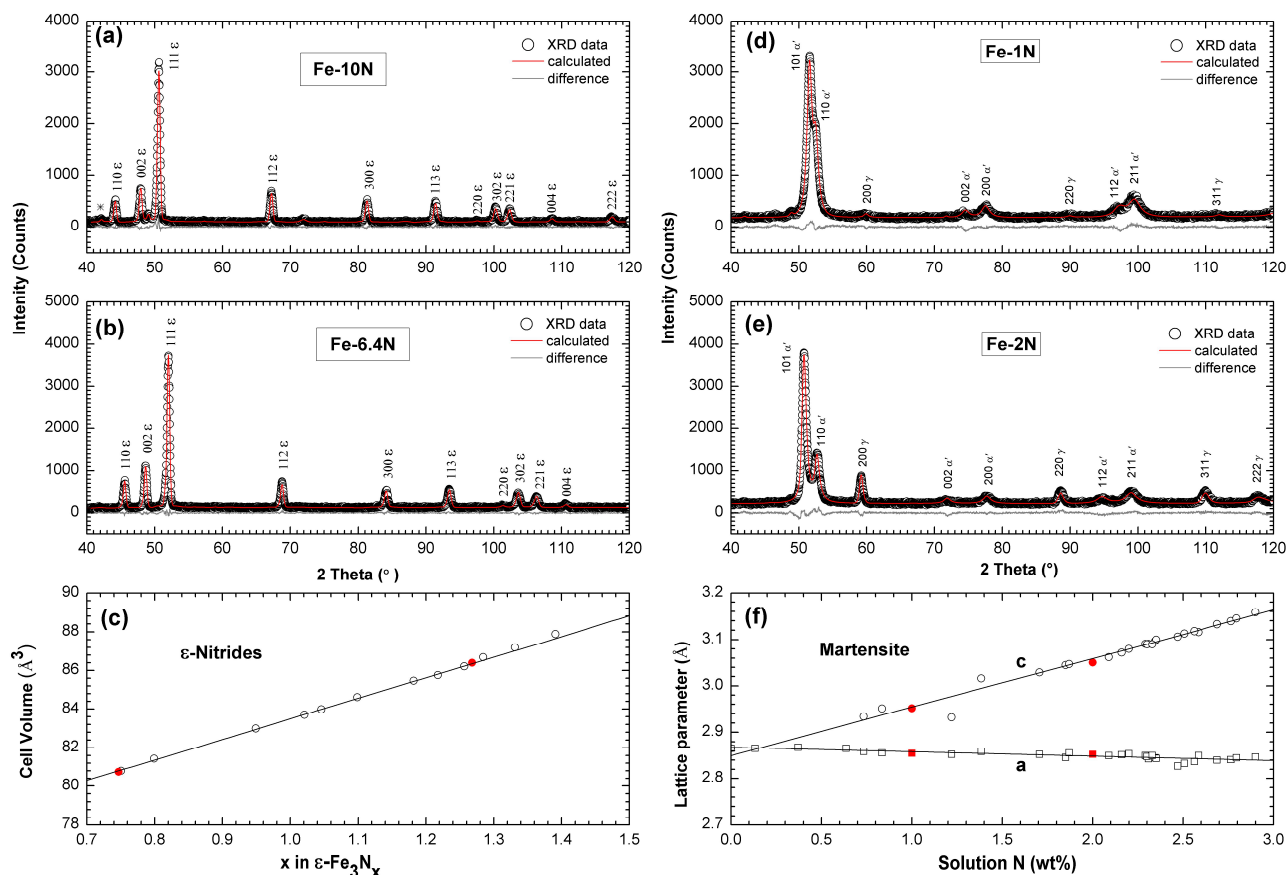


**Figure 3.** X-ray diffraction data of the recovered samples. (a), (b), (d), and (e) represent the diffraction patterns from Fe–10N, Fe–6.4N, Fe–1N, and Fe–2N compositions, respectively. The results of (a) and (b) show that Fe–10N and Fe–6.4N form a single nitride phase at 5 GPa and 1273 K. The diffraction patterns of (d) and (e) show that Fe–1N and Fe–2N samples mainly consist of the  $\alpha'$  phase with minor residual austenite ( $\gamma$ ), indicating that Fe–1N and Fe–2N are in the  $\gamma$  phase-field at 5 GPa and 1273 K. (c) shows the relationship between the unit-cell volume of nitrides and the x value in the formula  $\text{Fe}_3\text{N}_x$  with open circles [69] and solid circles (this study). (f) shows the lattice parameters c and a as a function of solution nitrogen in the Fe–N martensitic phase. The open symbols represent data from [84] and the solid symbols represent data from this study. Solid lines in (c) and (f) represent the linear fitting from the corresponding literature data.

**Table 1.** Phase constitutions, lattice parameters, and nitrogen concentrations calculated from the X-ray diffraction data of recovered samples at 5 GPa.

T (K)	$\epsilon$ -nitride						
	a (Å)	c (Å)	Volume (Å <sup>3</sup> )	Phase Fraction <sup>b</sup>	N Content (wt.%) <sup>c</sup>		
Fe-10N	1273	4.7581 (1) <sup>a</sup>	4.4066 (1)	86.3968 (37)	0.985 (15)	9.56 (14)	
Fe-6.4N	1273	4.6286 (2)	4.3521 (2)	80.7469 (105)	0.969 (15)	5.86 (9)	
		$\alpha'$ -Fe			$\gamma$ -Fe		
		a (Å)	c (Å)	Phase Fraction	a (Å)	Phase Fraction <sup>b</sup>	N Content (wt.%) <sup>d</sup>
Fe-1N	1273	2.8549 (1)	2.9514 (1)	0.932 (10)	3.5939 (1)	0.055 (11)	0.97 (2)
Fe-2N	1273	2.8509 (2)	3.0538 (1)	0.758 (12)	3.6259 (1)	0.239 (12)	1.95 (4)

<sup>a</sup> Numbers in parentheses refer to errors in the last digits; <sup>b</sup> Balance wüstite  $\text{FeO}_x$ ; <sup>c</sup> The N content in the  $\epsilon$ -nitride phase is determined by the relation between the experimental unit-cell volume and nitrogen content given by Liapina et al., 2004 [83]; <sup>d</sup> The N content in the solid solutions is determined by the relation between the nitrogen content and the lattice parameter c of the major martensitic phase given by Cheng et al., 1990 [84].

Figure 3d,e show the XRD data of the recovered samples from Fe–1N and Fe–2N compositions, indicating that both samples consist of the solid solution phases  $\alpha'$ -Fe (body-centered tetragonal structure, bct) and  $\gamma$ -Fe. The bct-structured  $\alpha'$ -Fe is a metastable phase formed by diffusionless transformation of the parent  $\gamma$ -Fe upon quenching. The result indicates that the compositions Fe–1N and Fe–2N are in the  $\gamma$  phase stability field at 5 GPa and 1273 K, with nitrogen alloying with Fe interstitially. This is the first time that the presence of the  $\alpha'$ -Fe–N phase has been recorded in the quenched sample from high-pressure experiments. Rietveld analysis further determined that Fe–2N contains much more residual  $\gamma$  phase compared to Fe–1N (Table 1), indicating that increasing the concentration of solute atomic N helps retain the  $\gamma$ -Fe phase at room temperature, similar to the observation in the Fe–C system [85,86]. Table 1 lists the lattice parameters of the martensitic and austenitic phases. We used the lattice parameter  $c$  of the major martensitic phase to calculate the N content in the recovered samples on the basis of the dependence of  $c$  on the solution N [84]. The calculation yielded 0.97(2) wt% N and 1.95(4) wt% N in Fe–1N and Fe–2N samples, respectively. It implies no detectable N loss in the heat-treated process at high pressure, in contrast to the behavior of nitrides. Figure 3f shows the lattice parameters of the Fe–N martensitic phase, along with the literature data [84], as a function of solution N content.

The XRD data indicate that at least 2 wt% N can be dissolved in  $\gamma$ -Fe at 5 GPa and 1273 K. Previous static high-pressure experiments have reported the  $\gamma$ -Fe phase containing N as high as ~2.1 wt% ( $\text{Fe}_4\text{N}_{0.35}$ ) at 19–30 GPa [69], which is comparable to the maximal N solubility of 2.7 wt% at 1 atm [75]. This suggests that pressure has a minor effect on the N solubility in  $\gamma$ -Fe, similar to the observation in the Fe–C system [85,86]. The high N solubility in solid Fe indicates that  $\gamma$ -Fe could be an important N-bearing phase in planetary cores besides nitrides.

### 3.3. Resistivity of Fe–N Compositions

Figure 4 shows the measured electrical resistivity of Fe–1N, Fe–2N, Fe–6.4N, and Fe–10N compositions as a function of temperature. The estimated error in sample temperature is ~50 K, along with ~2% uncertainty in resistivity. For comparison, the literature data concerning pure Fe at 1 atm [87] and 5 GPa [14,82], a recovered nitride  $\text{Fe}_2\text{N}$  at 1 atm [81], and Fe–Si alloys at 5 GPa [24,25] were also plotted in Figure 4. We specifically choose Fe–Si data for comparison due to similarities in Si content with our compositions, allowing a direct evaluation of the N effect on Fe resistivity. In addition, the resistivity data of Fe–Si alloys from different studies [22–26] are generally consistent compared to measurements for other compositions in the Fe–S, Fe–P and Fe–C systems. The data obtained at much higher pressures using diamond-anvil cells [17–21] were not included in the comparison.

All resistivity measurements were made during cooling after synthesizing a single phase at 5 GPa and high temperature. Except for the Fe–10N composition, the temperature dependence of the resistivity for Fe–1N, Fe–2N, and Fe–6.4N changes as the sample temperature decreases, indicating potential phase transitions. The implications for phase transitions will be discussed in the following sections. In this section, we focus on the effect of N on the resistivity of pure Fe, particularly at temperatures above 1000 K relevant to the thermal state in planetary interiors. Under these conditions, Fe–1N and Fe–2N are stable in the  $\gamma$  phase-field, while Fe–6.4N and Fe–10N form nitride phases according to our recovery experiments. As shown in Figure 4, N has a positive effect on the resistivity of Fe, similar to Si and other elements such as C, S, O, P, and H [29,30,33,38]. The resistivity of all Fe–N compositions shows a weak temperature dependence at high temperatures. The temperature dependence of Fe–1N and Fe–2N in  $\gamma$  phase is very similar to that of pure  $\gamma$ -Fe, with a temperature dependence of  $\frac{\partial \rho}{\partial T} \sim 0.045 \mu\Omega \cdot \text{cm K}^{-1}$ , whereas the nitride compositions exhibit lower temperature dependence with a value of  $\frac{\partial \rho}{\partial T} \sim 0.025 \mu\Omega \cdot \text{cm K}^{-1}$ , implying that the resistivity of the Fe–N system depends on both the N content and species. To further illustrate the influence of N on the Fe resistivity, we plotted the resistivity data of pure Fe and Fe–N compositions at 1273 K as a function of N content (Figure 5). The resistivity of

Fe–N solid solutions exhibits much more dependence on the N content compared to the nitrides. The linear fitting from the resistivity of pure Fe, Fe–1N, and Fe–2N shows a slope of 13.9  $\mu\Omega\cdot\text{cm}$  per weight percent N compared to a value of 3.78 for nitrides. This explicitly indicates that the interstitial N in solid metallic Fe plays a much more important role in changing the resistivity of Fe than that of nitrides.

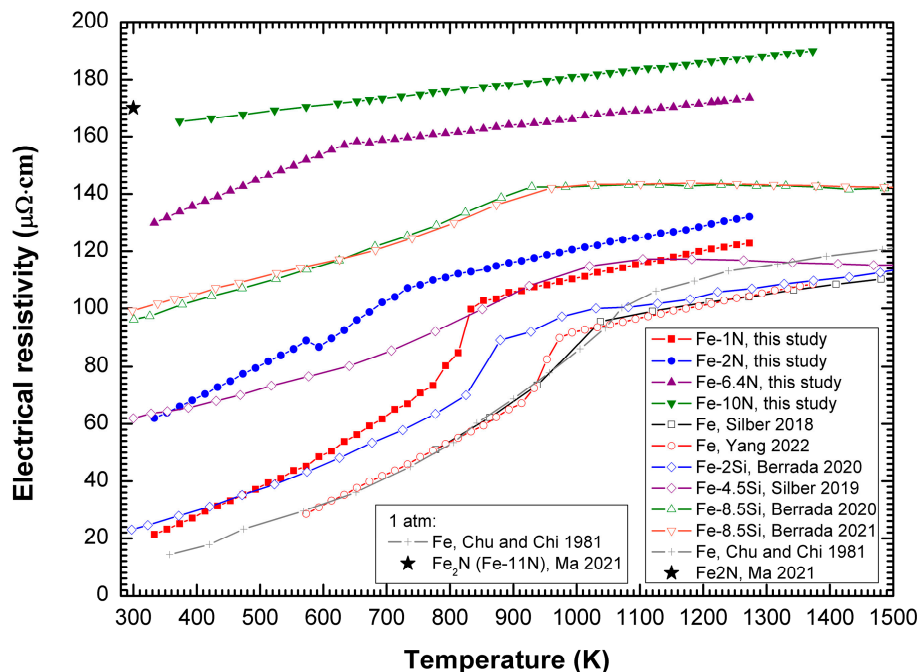


**Figure 4.** Resistivity of the four Fe–N compositions in this study, pure Fe [14,82], and Fe–Si [24–26] alloys at 5 GPa as a function of temperature. The resistivity of pure Fe at 1 atm [87] and the nitride  $\text{Fe}_2\text{N}$  under ambient conditions [81] are also plotted as gray cross and black star symbols, respectively, for comparison.

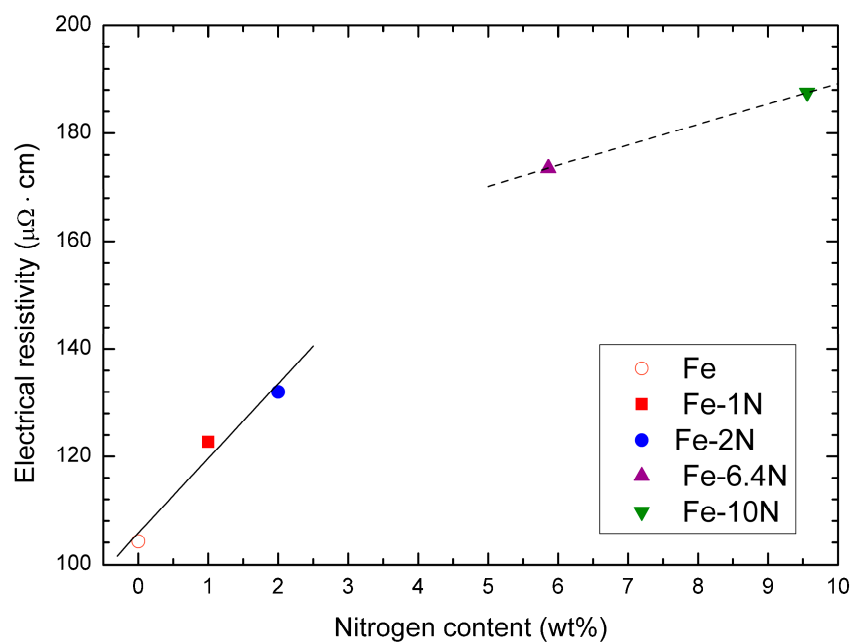


**Figure 5.** Resistivity of the four Fe–N compositions in this study and pure Fe [82] at 5 GPa and 1273 K as a function of nitrogen content. The solid line represents the linear fitting from the resistivity of pure Fe and Fe–N solid solutions, while the dashed line represents the linear fitting from the nitrides.

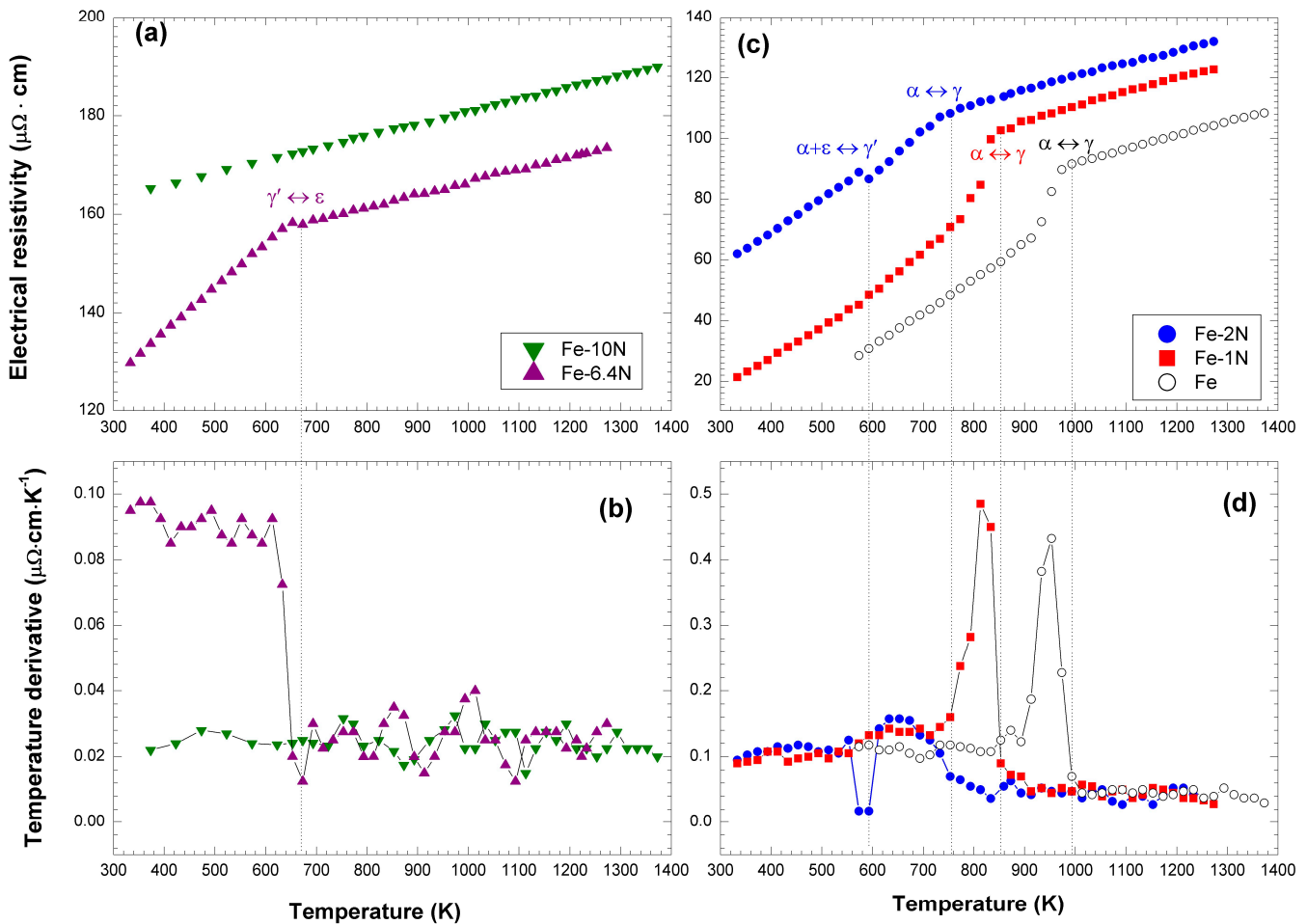
Comparing the effects of N and Si, N has a stronger effect on resistivity than Si (Figure 4). Fe–1N exhibits resistivity similar to Fe–4.5 wt%Si, and both Fe–1N and Fe–2N most likely have higher resistivity than Fe–8.5 wt%Si due to its negative temperature dependence at high temperature. The resistivity of the Fe–8.5 wt%Si alloy is ~20% and ~25% lower than nitrides Fe–6.4N and Fe–10N at 1273 K, respectively. The difference is enhanced when extrapolating to higher temperatures due to the negative temperature dependence of the solid Fe–Si alloys.

We also examined the validity of Matthiessen’s rule by calculating the elementary resistivity of N based on the experimental data. Matthiessen’s rule is usually used to describe the alloying effect of the solute atoms on the resistivity of pure metals [18,20,25,27,33,38,88]. This rule gives the resistivity  $\rho_{total}$  of dilute alloys as a sum of the resistivity of the pure metal matrix  $\rho_0(T)$  and the impurity term as a function of the solute concentration  $C_i$ ,  $\rho_{total}(C_i, T) = \rho_0(T) + \sum \rho_i C_i$ , where  $\rho_i$  is the elementary resistivity of solute  $i$ , which is only dependent on the impurity species. The calculated elementary resistivity  $\rho_i$  for Fe–1N is ~19  $\mu\Omega\cdot\text{cm}$  per weight percent N, different from the value ~14  $\mu\Omega\cdot\text{cm}$  for Fe–2N, indicating a deviation from Matthiessen’s rule.

Studies of the compression behavior of iron nitrides suggest that ~2.0–3.2 wt% N is required to explain the density deficit of the Earth’s inner core [69], while ~9.5 wt% is needed for the liquid outer core [70], assuming N is the sole core light element. However, considering the N budget in the bulk silicate Earth, the reasonable N content in the Earth’s core should be less than ~1 wt% based on the N abundance in CI chondrites (~3000 ppm by weight [48]). This content matches the N content of the metallic taenite phase in most iron meteorites [72]. Therefore, N is likely a minor component in the Earth’s core and possibly terrestrial planetary cores. Consequently, the minor N could be dissolved into the lattices of iron alloys such as Fe–Si (and/or, O, C, S) alloys and play an important role in controlling the transport properties of the planetary core, as shown by relatively higher electrical resistivity of the Fe–N alloys compared to the Fe–Si alloys (Figure 4). Models based on resistivity measurements in binary systems such as Fe–Si [17–26], Fe–S [27–32], and Fe–C [35] alloys may underestimate the resistivity and therefore overestimate the thermal conductivity of planetary cores if the role of N in the cores is ignored.

### 3.4. Phase Stability of $\gamma'$ -Fe<sub>4</sub>N at High Pressures

Phase transitions, such as decomposition and structure transformation, are usually accompanied by distinctive changes in resistivity. The resistivity data obtained in this study can be used to understand the phase evolution in the Fe–N system and the stability of  $\gamma'$ -Fe<sub>4</sub>N at high pressures. To elucidate the transition temperature, we calculated the temperature dependence of the resistivity using the formula,  $\frac{\partial \rho_i}{\partial T_i} = \frac{1}{2} \left( \frac{\rho_{i+1} - \rho_i}{T_{i+1} - T_i} + \frac{\rho_i - \rho_{i-1}}{T_i - T_{i-1}} \right)$ . Figure 6 shows the temperature dependence of the resistivity of the Fe–N alloys and iron nitrides during cooling. Fe–10N shows no apparent change in the temperature derivative as the temperature decreases from ~1400 K to near room temperature, indicating that the Fe–10N composition remains in the  $\epsilon$  phase at the investigated temperatures. In contrast, the Fe–6.4N composition shows a very strong change in the temperature derivative at ~673 K (Figure 6b). Our recovery experiment confirmed that the Fe–6.4N composition is in the  $\epsilon$  phase-field at 5 GPa and 1273 K (Figure 3b) and that the N content of the recovered sample (5.86 wt%) closely matches that of the  $\gamma'$ -Fe<sub>4</sub>N (~5.9 wt%). The phase diagram of the Fe–N system at 1 atm shows a transition point  $c$  at 953 K (Figure 7a), which indicates a congruent reaction of  $\epsilon \leftrightarrow \gamma'$ . Therefore, the observed change in the temperature derivative can be attributed to the  $\epsilon \leftrightarrow \gamma'$  transition. The transition temperature is ~280 K lower than that at 1 atm due to the pressure effect. The phase boundary shift is consistent with the  $\epsilon \leftrightarrow \gamma'$  congruent reaction temperature observed at 5 GPa in the recent work of Wetzel et al. [79].



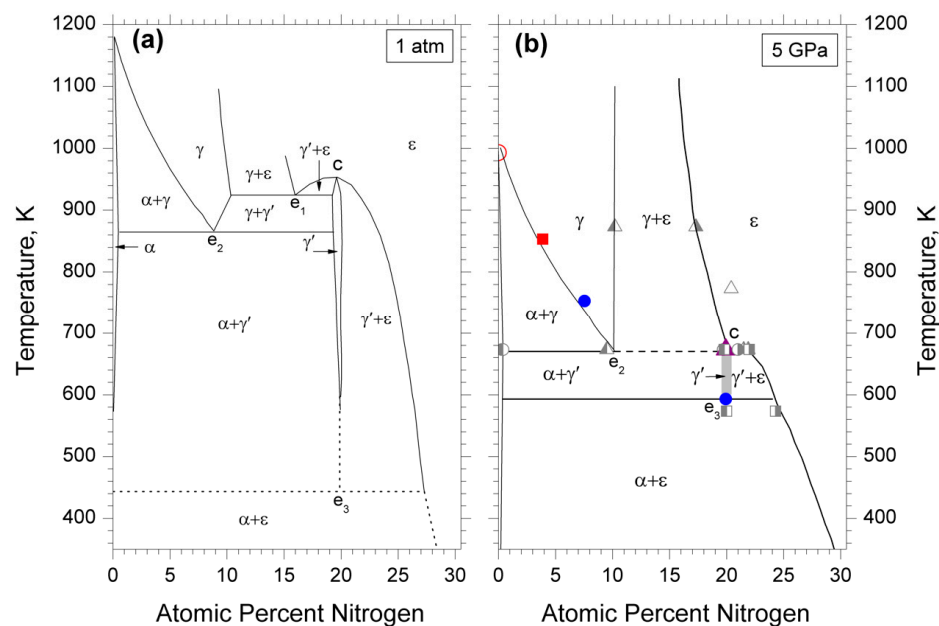
**Figure 6.** The resistivity of iron nitrides as a function of temperature (a) and its temperature derivative (b). The resistivity of Fe–N alloys as a function of temperature (c) and its temperature derivative (d). The vertical dot lines indicate the onset of the phase transition temperature. The allotropic and eutectoid reactions are marked near the transition points.

Figure 6c,d show the changes in the temperature derivative of the resistivity at ~955 K for pure Fe, ~853 K for Fe–1N, and ~753 K for Fe–2N. These changes correspond to the onset of the polymorphic transition  $\gamma \leftrightarrow \alpha$  [14,15,24–26,33,82,89,90]. The transition temperature decreases with the increasing N content, defining the  $\gamma \leftrightarrow \alpha + \gamma$  phase boundary (Figure 7b). Below the polymorphic transition temperature, a discontinuity is observed at ~593 K in the Fe–2N resistivity, likely attributed to the eutectoid reaction of  $\gamma' \leftrightarrow \alpha + \varepsilon$ . This decomposition reaction was theoretically predicted by Göhring et al. [74] (Figure 7a) but it has never been directly observed in experiments, possibly due to the sluggish reaction at low temperature.

Figure 7b shows a possible phase diagram at 5 GPa based on the phase diagram at 1 atm [74,75] and the recently reported phase equilibrium data at 4–6 GPa [79], combined with our phase transition points. The new experimental data provide constraints on the crucial phase transition boundary at high pressure. It is notable that the recovered samples reported by Wetzel et al. [79] frequently contained three or even four phases, suggesting a non-equilibrium assemblage probably due to the slow kinetics at low temperatures. We only used the data from the equilibrium assemblage to construct Figure 7b. In the Fe-rich region, the three polymorphic transition points determined from the resistivity measurements of pure Fe, Fe–1N, and Fe–2N constrain a boundary of an  $\alpha + \gamma$  dual-phase region in equilibrium with the  $\gamma$  phase at 5 GPa. This boundary shifts toward the low temperature by ~200 K compared with that at 1 atm. The congruent transition  $\varepsilon \leftrightarrow \gamma'$  of Fe–6.4N at ~673 K determines the highest temperature for the stability of  $\gamma'$ -Fe<sub>4</sub>N. It, along

with the literature phase data, defines a new congruent point marked as  $c$  in Figure 7b. The discontinuity at  $\sim 593$  K from the Fe–2N resistivity measurements is proposed as the eutectoid reaction  $\gamma' \leftrightarrow \alpha + \varepsilon$  ( $e_3$ ). No discontinuity is observed from the Fe–6.4N and Fe–1N resistivity data, which is likely due to the slow kinetics of the eutectoid decomposition of  $\gamma'$ -Fe<sub>4</sub>N. The phase retention caused by the hysteretic effect usually leads to nonequilibrium phase recovery as found in the work of Wetzel et al. [79]. The lack of a detectable eutectoid reaction of  $\gamma \leftrightarrow \alpha + \gamma'$  ( $e_2$ ) in the Fe–1N and Fe–2N resistivity measurements is likely due to the nonequilibrium retention of the  $\gamma$  phase and the narrow temperature interval between the eutectoid reaction  $\gamma \leftrightarrow \alpha + \gamma'$  and the polymorphic transition  $\gamma \leftrightarrow \alpha$ . Further detailed experiments are needed to refine the transition temperatures.

The phase-field of  $\gamma'$ -Fe<sub>4</sub>N is contracted at 5 GPa, suggesting that the  $\gamma'$ -Fe<sub>4</sub>N phase may disappear at higher pressure. Wetzel et al. (2021) [79] derived a reaction path for the pressure-induced disappearance of the  $\gamma'$ -Fe<sub>4</sub>N phase. They argued that the eutectoid reaction  $\varepsilon \leftrightarrow \gamma + \gamma'$  ( $e_1$ ) would coincide with the congruent reaction  $\varepsilon \leftrightarrow \gamma'$  ( $c$ ) at  $\sim 4$  GPa, accompanying the disappearance of the dual-phase region of  $\gamma' + \varepsilon$  and the appearance of a peritectoid reaction  $\gamma + \varepsilon \leftrightarrow \gamma'$ . At pressures above  $\sim 5$  GPa, the eutectoid reactions  $\gamma \leftrightarrow \alpha + \gamma'$  ( $e_2$ ) and  $\gamma' \leftrightarrow \alpha + \varepsilon$  ( $e_3$ ) and the peritectoid reaction  $\gamma + \varepsilon \leftrightarrow \gamma'$  would coincide in a quadruple point, leaving a new eutectoid reaction  $\gamma \leftrightarrow \alpha + \varepsilon$ . According to the path, they proposed that  $\gamma'$ -Fe<sub>4</sub>N is a metastable phase and unlikely to occur in the Fe–N system at pressures exceeding 10 GPa. Further experiments are needed to conclusively determine the stability of  $\gamma'$ -Fe<sub>4</sub>N. However,  $\gamma'$ -Fe<sub>4</sub>N is unlikely as the N-bearing phase in the cores of planetary bodies such as Earth, the Moon, Mercury, and Ganymede because it is observed at too low a temperature at core pressures.



**Figure 7.** The phase relations in the Fe–N binary system. (a) The phase diagram of the Fe–N system at ambient pressure adopted from Wriedt et al. [75]. At low temperatures, an  $\alpha + \varepsilon$  equilibrium predicted by Gohring et al. [74] is also plotted with dash lines. (b) The proposed phase relations in the Fe–N system at 5 GPa. The solid symbols (square, circle, and triangle) represent the transition temperatures determined using the resistivity measurements of this study. Recently reported phase equilibrium data at 4–6 GPa [79] are plotted using gray symbols. The open gray triangle represents the  $\varepsilon$ -nitride single phase. The gray half-filled symbols represent two-phase coexistence (circles:  $\alpha + \gamma'$ ; squares:  $\gamma' + \varepsilon$ ; triangles:  $\gamma + \varepsilon$ ). The isotherm  $e_2c$  is plotted with a dashed line to show it is not in equilibrium (see the main text).

#### 4. Conclusions

In conclusion, our high-pressure experiments at 5 GPa and up to 1400 K in the Fe–N system, including the solid solutions Fe–1 wt%N and Fe–2 wt%N and nitrides Fe–6.4 wt%N and Fe–10 wt%N, have provided valuable insights into the electrical resistivity behavior and phase relations in the Fe–N system. We observed weak temperature dependence in the resistivity of all compositions. The recovery experiments indicated that the solid solutions reside in the  $\gamma$  phase-field, while two nitrides are in the  $\epsilon$  phase-field at 5 GPa and 1273 K. Our data highlighted the significant influence of nitrogen impurities on the resistivity of Fe, particularly interstitial nitrogen, surpassing the effect of Si. Notably, alloying with 1 wt% N shows higher resistivity than alloying with 4.5 wt% Si and possibly 8.5 wt% Si. Further experiments are needed to explore the resistivity of ternary compositions such as Fe–N–Si, Fe–N–C, and Fe–N–O and to comprehensively evaluate the impurity effect of N in complex systems. Furthermore, our temperature-dependent resistivity data allowed determination of the phase evolution of the Fe–N system at high pressures. On the basis of the changes in the temperature dependence of the measured resistivity combined with the literature phase equilibrium data, we proposed a phase diagram in the Fe–N binary system at 5 GPa. This phase diagram features a contracted  $\gamma'$ -Fe<sub>4</sub>N field compared to that at 1 atm. Taking the recent phase equilibrium study into account, we concluded that the fcc nitride  $\gamma'$ -Fe<sub>4</sub>N is unlikely to be the N-bearing phase present in planetary cores. Instead, the likely dominant N-bearing phase is  $\gamma$ -Fe, with dissolved N up to ~2 wt%. To further elucidate the phase relations in the Fe–N system, it is necessary to study the melting relations and the resistivity measurements of the Fe–N melts, which will provide insights into the composition and dynamic evolution of planetary cores.

**Author Contributions:** Conceptualization, X.H. and Y.F.; Funding acquisition, Y.F.; Investigation, Y.W. and F.Y.; Resources, X.H.; Software, C.S.; Supervision, X.H. and Y.F.; Writing—original draft, Y.W.; Writing—review and editing, J.Y., X.H. and Y.F. All authors have read and agreed to the published version of the manuscript.

**Funding:** This study is supported by National Natural Science Foundation of China under Grants U1330111 and 41404067.

**Data Availability Statement:** The data that supports the findings of this study are available within the article.

**Conflicts of Interest:** The authors declare no conflicts of interest.

#### References

1. Driscoll, P.; Davies, C. The “new core paradox”: Challenges and potential solutions. *J. Geophys. Res. Solid Earth* **2023**, *128*, e2022JB025355. [[CrossRef](#)]
2. Nimmo, F. Energetics of the Core. In *Treatise on Geophysics*, 2nd ed.; Schubert, G., Ed.; Elsevier: Oxford, UK, 2015; pp. 27–55.
3. Breuer, D.; Rueckriemen, T.; Spohn, T. Iron snow, crystal floats, and inner-core growth: Modes of core solidification and implications for dynamos in terrestrial planets and moons. *Prog. Earth Planet. Sci.* **2015**, *2*, 39. [[CrossRef](#)]
4. Zhou, Y.; Dong, Z.; Hsieh, W.-P.; Goncharov, A.; Chen, X.-J. Thermal conductivity of materials under pressure. *Nat. Rev. Phys.* **2022**, *4*, 319–335. [[CrossRef](#)]
5. Zurkowski, C.C.; Fei, Y. Mineralogy of Planetary Cores. In *Celebrating the International Year of Mineralogy: Progress and Landmark Discoveries of the Last Decades*; Bindi, L., Cruciani, G., Eds.; Springer Nature Switzerland: Cham, Switzerland, 2023; pp. 207–247.
6. Hirose, K.; Wood, B.; Vočadlo, L. Light elements in the Earth’s core. *Nat. Rev. Earth Environ.* **2021**, *2*, 645–658. [[CrossRef](#)]
7. Ohta, K.; Suehiro, S.; Kawaguchi, S.I.; Okuda, Y.; Wakamatsu, T.; Hirose, K.; Ohishi, Y.; Kodama, M.; Hirai, S.; Azuma, S. Measuring the electrical resistivity of liquid iron to 1.4 Mbar. *Phys. Rev. Lett.* **2023**, *130*, 266301. [[CrossRef](#)] [[PubMed](#)]
8. Zhang, Y.; Hou, M.; Liu, G.; Zhang, C.; Prakapenka, V.B.; Greenberg, E.; Fei, Y.; Cohen, R.E.; Lin, J.-F. Reconciliation of experiments and theory on transport properties of iron and the geodynamo. *Phys. Rev. Lett.* **2020**, *125*, 078501. [[CrossRef](#)] [[PubMed](#)]
9. Suehiro, S.; Wakamatsu, T.; Ohta, K.; Hirose, K.; Ohishi, Y. High-temperature electrical resistivity measurements of hcp iron to Mbar pressure in an internally resistive heated diamond anvil cell. *High Press. Res.* **2019**, *39*, 579–587. [[CrossRef](#)]
10. Ohta, K.; Kuwayama, Y.; Hirose, K.; Shimizu, K.; Ohishi, Y. Experimental determination of the electrical resistivity of iron at Earth’s core conditions. *Nature* **2016**, *534*, 95–98. [[CrossRef](#)] [[PubMed](#)]
11. Gomi, H.; Ohta, K.; Hirose, K.; Labrosse, S.; Caracas, R.; Verstraete, M.J.; Hernlund, J.W. The high conductivity of iron and thermal evolution of the Earth’s core. *Phys. Earth Planet. Inter.* **2013**, *224*, 88–103. [[CrossRef](#)]

12. Deng, L.; Seagle, C.; Fei, Y.; Shahar, A. High pressure and temperature electrical resistivity of iron and implications for planetary cores. *Geophys. Res. Lett.* **2013**, *40*, 33–37. [[CrossRef](#)]
13. Secco, R.A.; Schloessin, H.H. The electrical resistivity of solid and liquid Fe at pressures up to 7 GPa. *J. Geophys. Res. Solid Earth* **1989**, *94*, 5887–5894. [[CrossRef](#)]
14. Silber, R.; Secco, R.; Yong, W.; Littleton, J. Electrical resistivity of liquid Fe to 12 GPa: Implications for heat flow in cores of terrestrial bodies. *Sci. Rep.* **2018**, *8*, 10758. [[CrossRef](#)] [[PubMed](#)]
15. Ezenwa, I.C.; Yoshino, T. Technique, cell assembly, and measurement of T-dependent electrical resistivity of liquid Fe devoid of contamination at P, T conditions. *Rev. Sci. Instrum.* **2020**, *91*, 023903. [[CrossRef](#)] [[PubMed](#)]
16. Yong, W.; Secco, R.A.; Littleton, J.A.H.; Silber, R.E. The iron invariance: Implications for thermal convection in Earth's core. *Geophys. Res. Lett.* **2019**, *46*, 11065–11070. [[CrossRef](#)]
17. Zhang, Y.; Luo, K.; Hou, M.; Driscoll, P.; Salke, N.P.; Minár, J.; Prakapenka, V.B.; Greenberg, E.; Hemley, R.J.; Cohen, R.E.; et al. Thermal conductivity of Fe-Si alloys and thermal stratification in Earth's core. *Proc. Natl. Acad. Sci. USA* **2022**, *119*, e2119001119. [[CrossRef](#)] [[PubMed](#)]
18. Zhang, Y.; Hou, M.; Driscoll, P.; Salke, N.P.; Liu, J.; Greenberg, E.; Prakapenka, V.B.; Lin, J.-F. Transport properties of Fe-Ni-Si alloys at Earth's core conditions: Insight into the viability of thermal and compositional convection. *Earth Planet. Sci. Lett.* **2021**, *553*, 116614. [[CrossRef](#)]
19. Inoue, H.; Suehiro, S.; Ohta, K.; Hirose, K.; Ohishi, Y. Resistivity saturation of hcp Fe-Si alloys in an internally heated diamond anvil cell: A key to assessing the Earth's core conductivity. *Earth Planet. Sci. Lett.* **2020**, *543*, 116357. [[CrossRef](#)]
20. Gomi, H.; Hirose, K.; Akai, H.; Fei, Y. Electrical resistivity of substitutionally disordered hcp Fe-Si and Fe-Ni alloys: Chemically-induced resistivity saturation in the Earth's core. *Earth Planet. Sci. Lett.* **2016**, *451*, 51–61. [[CrossRef](#)]
21. Seagle, C.; Fei, Y.; Cottrell, E.; Hummer, D.; Prakapenka, V. Electrical and thermal transport properties of iron and iron-silicon alloy at high pressure. *Geophys. Res. Lett.* **2013**, *40*, 5377–5381. [[CrossRef](#)]
22. Lenhart, E.M.; Yong, W.; Secco, R.A.; Flemming, R. Electrical resistivity of liquid Fe-8wt%S-4.5wt%Si at high pressures with implications for heat flux through the cores of Io and sub-earth exoplanets. *Icarus* **2023**, *395*, 115472. [[CrossRef](#)]
23. Berrada, M.; Secco, R.A.; Yong, W. Resistivity of solid and liquid Fe-Ni-Si with applications to the cores of Earth. *Mercury Venus Sci. Rep.* **2022**, *12*, 9941. [[PubMed](#)]
24. Berrada, M.; Secco, R.A.; Yong, W. Adiabatic heat flow in Mercury's core from electrical resistivity measurements of liquid Fe-8.5 wt% Si to 24 GPa. *Earth Planet. Sci. Lett.* **2021**, *568*, 117053. [[CrossRef](#)]
25. Berrada, M.; Secco, R.A.; Yong, W.; Littleton, J.A.H. Electrical resistivity measurements of Fe-Si with implications for the early Lunar dynamo. *J. Geophys. Res. Planets* **2020**, *125*, e2020JE006380. [[CrossRef](#)]
26. Silber, R.E.; Secco, R.A.; Yong, W.; Littleton, J.A.H. Heat flow in Earth's core from invariant electrical resistivity of Fe-Si on the melting boundary to 9 GPa: Do light elements matter? *J. Geophys. Res. Solid Earth* **2019**, *124*, 5521–5543. [[CrossRef](#)]
27. Suehiro, S.; Ohta, K.; Hirose, K.; Morard, G.; Ohishi, Y. The influence of sulfur on the electrical resistivity of hcp iron: Implications for the core conductivity of Mars and Earth. *Geophys. Res. Lett.* **2017**, *44*, 8254–8259. [[CrossRef](#)]
28. Saxena, S.; Pommier, A.; Tauber, M.J. Iron sulfides and anomalous electrical resistivity in Cratonic environments. *J. Geophys. Res. Solid Earth* **2021**, *126*, e2021JB022297. [[CrossRef](#)]
29. Littleton, J.A.H.; Secco, R.A.; Yong, W. Electrical resistivity of FeS at high pressures and temperatures: Implications of thermal transport in the core of Ganymede. *J. Geophys. Res. Planets* **2021**, *126*, e2020JE006793. [[CrossRef](#)]
30. Pommier, A. Experimental investigation of the effect of nickel on the electrical resistivity of Fe-Ni and Fe-Ni-S alloys under pressure. *Am. Mineral. J. Earth Planet. Mater.* **2020**, *105*, 1069–1077. [[CrossRef](#)]
31. Manthilake, G.; Chantel, J.; Monteux, J.; Andrault, D.; Bouhifd, M.A.; Casanova, N.B.; Boulard, E.; Guignot, N.; King, A.; Itie, J.P. Thermal conductivity of FeS and its implications for Mercury's long-sustaining magnetic field. *J. Geophys. Res. Planets* **2019**, *124*, 2359–2368. [[CrossRef](#)]
32. Pommier, A. Influence of sulfur on the electrical resistivity of a crystallizing core in small terrestrial bodies. *Earth Planet. Sci. Lett.* **2018**, *496*, 37–46. [[CrossRef](#)]
33. Yin, Y.; Wang, L.; Zhai, S.; Fei, Y. Electrical resistivity of Fe and Fe-3 wt%P at 5 GPa with implications for the Moon's core conductivity and dynamo. *J. Geophys. Res. Planets* **2022**, *127*, e2021JE007116. [[CrossRef](#)]
34. Yin, Y.; Zhai, K.; Zhang, B.; Zhai, S. Electrical resistivity of iron phosphides at high-pressure and high-temperature conditions with implications for Lunar core's thermal conductivity. *J. Geophys. Res. Solid Earth* **2019**, *124*, 5544–5556. [[CrossRef](#)]
35. Zhang, C.; Lin, J.-F.; Liu, Y.; Feng, S.; Jin, C.; Hou, M.; Yoshino, T. Electrical resistivity of Fe-C alloy at high pressure: Effects of carbon as a light element on the thermal conductivity of the Earth's core. *J. Geophys. Res. Solid Earth* **2018**, *123*, 3564–3577. [[CrossRef](#)]
36. Ramakrishna, K.; Lokamani, M.; Baczewski, A.; Vorberger, J.; Cangi, A. Electrical conductivity of iron in Earth's core from microscopic Ohm's law. *Phys. Rev. B* **2023**, *107*, 115131. [[CrossRef](#)]
37. Kleinschmidt, U.; French, M.; Steinle-Neumann, G.; Redmer, R. Electrical and thermal conductivity of fcc and hcp iron under conditions of the Earth's core from ab initio simulations. *Phys. Rev. B* **2023**, *107*, 085145. [[CrossRef](#)]
38. Gomi, H.; Hirose, K. Impurity resistivity of the Earth's inner core. *J. Geophys. Res. Solid Earth* **2023**, *128*, e2023JB027097. [[CrossRef](#)]
39. Pozzo, M.; Davies, C.J.; Alfè, D. Towards reconciling experimental and computational determinations of Earth's core thermal conductivity. *Earth Planet. Sci. Lett.* **2022**, *584*, 117466. [[CrossRef](#)]

40. Xu, J.; Zhang, P.; Haule, K.; Minar, J.; Wimmer, S.; Ebert, H.; Cohen, R.E. Thermal conductivity and electrical resistivity of solid iron at Earth's core conditions from first principles. *Phys. Rev. Lett.* **2018**, *121*, 096601. [[CrossRef](#)] [[PubMed](#)]
41. Pozzo, M.; Davies, C.; Gubbins, D.; Alfè, D. Thermal and electrical conductivity of solid iron and iron-silicon mixtures at Earth's core conditions. *Earth Planet. Sci. Lett.* **2014**, *393*, 159–164. [[CrossRef](#)]
42. Pozzo, M.; Davies, C.; Gubbins, D.; Alfè, D. Thermal and electrical conductivity of iron at Earth's core conditions. *Nature* **2012**, *485*, 355–358. [[CrossRef](#)]
43. de Koker, N.; Steinle-Neumann, G.; Vlcek, V. Electrical resistivity and thermal conductivity of liquid Fe alloys at high P and T, and heat flux in Earth's core. *Proc. Natl. Acad. Sci. USA* **2012**, *109*, 4070–4073. [[CrossRef](#)] [[PubMed](#)]
44. Wagle, F.; Steinle-Neumann, G.; de Koker, N. Saturation and negative temperature coefficient of electrical resistivity in liquid iron-sulfur alloys at high densities from first-principles calculations. *Phys. Rev. B* **2018**, *97*, 094307. [[CrossRef](#)]
45. Li, Q.; Xian, J.-W.; Zhang, Y.; Sun, T.; Vočadlo, L. Thermal properties of liquid iron at conditions of planetary cores. *J. Geophys. Res. Planets* **2022**, *127*, e2021JE007015. [[CrossRef](#)]
46. Naka, M.; Masumoto, T.; Imai, Y. Solubility of nitrogen in austenitic iron under high pressure of nitrogen gas and thermodynamical properties of austenitic interstitial solid solution of the Fe-N System. *J. Jpn. Inst. Met.* **1970**, *34*, 195–201.
47. Ishii, F.; Ban-Ya, S.; Fuwa, T. Solubility of nitrogen in liquid iron alloys. *Tetsu-to-Hagané* **1982**, *68*, 1551–1559. [[CrossRef](#)]
48. McDonough, W.F.; Sun, S.S. The composition of the Earth. *Chem. Geol.* **1995**, *120*, 223–253. [[CrossRef](#)]
49. Allègre, C.; Manhès, G.; Lewin, É. Chemical composition of the Earth and the volatility control on planetary genetics. *Earth Planet. Sci. Lett.* **2001**, *185*, 49–69. [[CrossRef](#)]
50. Johnson, B.; Goldblatt, C. The nitrogen budget of Earth. *Earth-Sci. Rev.* **2015**, *148*, 150–173. [[CrossRef](#)]
51. Halliday, A.N. The origins of volatiles in the terrestrial planets. *Geochim. Cosmochim. Acta* **2013**, *105*, 146–171. [[CrossRef](#)]
52. Marty, B. The origins and concentrations of water, carbon, nitrogen and noble gases on Earth. *Earth Planet. Sci. Lett.* **2012**, *313*, 56–66. [[CrossRef](#)]
53. Bergin, E.A.; Blake, G.A.; Ciesla, F.; Hirschmann, M.M.; Li, J. Tracing the ingredients for a habitable earth from interstellar space through planet formation. *Proc. Natl. Acad. Sci. USA* **2015**, *112*, 8965–8970. [[CrossRef](#)] [[PubMed](#)]
54. Alexander, C.M.O.D.; Howard, K.T.; Bowden, R.; Fogel, M.L. The classification of CM and CR chondrites using bulk H, C and N abundances and isotopic compositions. *Geochim. Cosmochim. Acta* **2013**, *123*, 244–260. [[CrossRef](#)]
55. Grady, M.M.; Wright, I.P. Elemental and isotopic abundances of carbon and nitrogen in meteorites. *Space Sci. Rev.* **2003**, *106*, 231–248. [[CrossRef](#)]
56. Hirschmann, M.M. Constraints on the early delivery and fractionation of Earth's major volatiles from C/H, C/N, and C/S ratios. *Am. Mineral.* **2016**, *101*, 540–553. [[CrossRef](#)]
57. Tucker, J.M.; Mukhopadhyay, S. Evidence for multiple magma ocean outgassing and atmospheric loss episodes from mantle noble gases. *Earth Planet. Sci. Lett.* **2014**, *393*, 254–265. [[CrossRef](#)]
58. Speilmanns, I.M.; Schmidt, M.W.; Liebske, C. The almost lithophile character of nitrogen during core formation. *Earth Planet. Sci. Lett.* **2019**, *510*, 186–197. [[CrossRef](#)]
59. Roskosz, M.; Bouhifd, M.A.; Jephcoat, A.P.; Marty, B.; Mysen, B.O. Nitrogen solubility in molten metal and silicate at high pressure and temperature. *Geochim. Cosmochim. Acta* **2013**, *121*, 15–28. [[CrossRef](#)]
60. Li, Y.; Wiedenbeck, M.; Monteleone, B.; Dasgupta, R.; Costin, G.; Gao, Z.; Lu, W. Nitrogen and carbon fractionation in planetary magma oceans and origin of the superchondritic C/N ratio in the bulk silicate Earth. *Earth Planet. Sci. Lett.* **2023**, *605*, 118032. [[CrossRef](#)]
61. Grewal, D.S.; Dasgupta, R.; Hough, T.; Farnell, A. Rates of protoplanetary accretion and differentiation set nitrogen budget of rocky planets. *Nat. Geosci.* **2021**, *14*, 369–376. [[CrossRef](#)]
62. Speilmanns, I.M.; Schmidt, M.W.; Liebske, C. Nitrogen solubility in core materials. *Geophys. Res. Lett.* **2018**, *45*, 7434–7443. [[CrossRef](#)]
63. Dalou, C.; Hirschmann, M.M.; von der Handt, A.; Mosenfelder, J.; Armstrong, L.S. Nitrogen and carbon fractionation during core-mantle differentiation at shallow depth. *Earth Planet. Sci. Lett.* **2017**, *458*, 141–151. [[CrossRef](#)]
64. Jackson, C.R.M.; Cottrell, E.; Du, Z.; Bennett, N.R.; Fei, Y. High pressure redistribution of nitrogen and sulfur during planetary stratification. *Geochim. Perspect. Lett.* **2021**, *18*, 37–42. [[CrossRef](#)]
65. Lv, C.; Liu, J. Ultralow melting of iron nitrides and the Fe-N-C system at high pressure. *J. Geophys. Res. Solid Earth* **2022**, *127*, e2021JB023718. [[CrossRef](#)]
66. Lv, M.; Liu, J.; Zhu, F.; Li, J.; Zhang, D.; Xiao, Y.; Dorfman, S.M. Spin transitions and compressibility of  $\epsilon$ -Fe<sub>7</sub>N<sub>3</sub> and  $\gamma'$ -Fe<sub>4</sub>N: Implications for iron alloys in terrestrial planet cores. *J. Geophys. Res. Solid Earth* **2020**, *125*, e2020JB020660. [[CrossRef](#)]
67. Kusakabe, M.; Hirose, K.; Sinmyo, R.; Kuwayama, Y.; Ohishi, Y.; Helffrich, G. Melting curve and equation of state of  $\beta$ -Fe<sub>7</sub>N<sub>3</sub>: Nitrogen in the core? *J. Geophys. Res. Solid Earth* **2019**, *124*, 3448–3457. [[CrossRef](#)]
68. Breton, H.; Komabayashi, T.; Thompson, S.; Potts, N.; McGuire, C.; Suehiro, S.; Anzellini, S.; Ohishi, Y. Static compression of Fe<sub>4</sub>N to 77 GPa and its implications for nitrogen storage in the deep Earth. *Am. Mineral.* **2019**, *104*, 1781–1787. [[CrossRef](#)]
69. Litasov, K.D.; Shatskiy, A.; Ponomarev, D.S.; Gavryushkin, P.N. Equations of state of iron nitrides  $\epsilon$ -Fe<sub>3</sub>N<sub>x</sub> and  $\gamma$ -Fe<sub>4</sub>N<sub>y</sub> to 30 GPa and 1200 K and implication for nitrogen in the Earth's core. *J. Geophys. Res.* **2017**, *122*, 3574–3584. [[CrossRef](#)]
70. Minobe, S.; Nakajima, Y.; Hirose, K.; Ohishi, Y. Stability and compressibility of a new iron-nitride  $\beta$ -Fe<sub>7</sub>N<sub>3</sub> to core pressures. *Geophys. Res. Lett.* **2015**, *42*, 5206–5211. [[CrossRef](#)]

71. Adler, J.F.; Williams, Q. A high-pressure X-ray diffraction study of iron nitrides: Implications for Earth's core. *J. Geophys. Res. Solid Earth* **2005**, *110*, 1–11. [[CrossRef](#)]
72. Sugiura, N. Ion probe measurements of carbon and nitrogen in iron meteorites. *Meteorit. Planet. Sci.* **1998**, *33*, 393–409. [[CrossRef](#)]
73. Sharygin, V.V.; Ripp, G.S.; Yakovlev, G.A.; Seryotkin, Y.V.; Karmanov, N.S.; Izbrodin, I.A.; Grokhovsky, V.I.; Khromova, E.A. Uakitite, VN, a new mononitride mineral from Uakit iron meteorite (IIAB). *Minerals* **2020**, *10*, 150. [[CrossRef](#)]
74. Göhring, H.; Fabrichnaya, O.; Leineweber, A.; Mittemeijer, E.J. Thermodynamics of the Fe-N and Fe-N-C systems: The Fe-N and Fe-N-C phase diagrams revisited. *Metall. Mater. Trans. A* **2016**, *47*, 6173–6186. [[CrossRef](#)]
75. Wriedt, H.A.; Gokcen, N.A.; Nafziger, R.H. The Fe-N (Iron-Nitrogen) system. *Bull. Alloy Phase Diagr.* **1987**, *8*, 355–377. [[CrossRef](#)]
76. Zhuang, Y.; Su, X.; Salke, N.P.; Cui, Z.; Hu, Q.; Zhang, D.; Liu, J. The effect of nitrogen on the compressibility and conductivity of iron at high pressure. *Geosci. Front.* **2021**, *12*, 983–989. [[CrossRef](#)]
77. Bajgain, S.K.; Mookherjee, M.; Dasgupta, R.; Ghosh, D.; Karki, B.B. Nitrogen content in the Earth's outer core. *Geophys. Res. Lett.* **2019**, *46*, 88–98. [[CrossRef](#)]
78. Guo, K.; Rau, D.; Von Appen, J.; Prots, Y.; Schnelle, W.; Dronskowski, R.; Niewa, R.; Schwarz, U. High pressure high-temperature behavior and magnetic properties of Fe<sub>4</sub>N: Experiment and theory. *High Press. Res.* **2013**, *33*, 684–696. [[CrossRef](#)]
79. Wetzel, M.; Rabending, T.; Friák, M.; Všíanská, M.; Sob, M.; Leineweber, A. Phase stability of iron nitride Fe<sub>4</sub>N at high pressure-pressure-dependent evolution of phase equilibria in the Fe-N system. *Materials* **2021**, *14*, 3963. [[CrossRef](#)] [[PubMed](#)]
80. Wetzel, M.H.; Schwarz, M.R.; Leineweber, A. High-pressure high-temperature study of the pressure induced decomposition of the iron nitride  $\gamma'$ -Fe<sub>4</sub>N. *J. Alloys Compd.* **2019**, *801*, 438–448. [[CrossRef](#)]
81. Ma, T.; Yin, Y.; Hong, F.; Zhu, P.; Yu, X. Magnetic, electronic, and mechanical properties of bulk  $\epsilon$ -Fe<sub>2</sub>N synthesized at high pressures. *ACS Omega* **2021**, *6*, 12591–12597. [[CrossRef](#)]
82. Yang, F.; Hu, X.; Fei, Y. In Situ measurements of electrical resistivity of metals in a cubic multi-anvil apparatus by van der Pauw method. *Rev. Sci. Instrum.* **2022**, *93*, 053902. [[CrossRef](#)]
83. Liapina, T.; Leineweber, A.; Mittemeijer, E.; Kockelmann, W. The lattice parameters of  $\epsilon$ -iron nitrides: Lattice strains due to a varying degree of nitrogen ordering. *Acta Mater.* **2004**, *52*, 173–180. [[CrossRef](#)]
84. Cheng, L.; Böttger, A.; de Keijser, T.H.; Mittemeijer, E.J. Lattice parameters of iron-carbon and iron-nitrogen martensites and austenites. *Scr. Metall. Et Mater.* **1990**, *24*, 509–514. [[CrossRef](#)]
85. Yang, J.; Fei, Y.; Hu, X.; Greenberg, E.; Prakapenka, V.B. Effect of carbon on the volume of solid iron at high pressure: Implications for carbon substitution in iron structures and carbon content in the Earth's inner core. *Minerals* **2019**, *9*, 720. [[CrossRef](#)]
86. Fei, Y.; Brosh, E. Experimental study and thermodynamic calculations of phase relations in the Fe-C system at high pressure. *Earth Planet. Sci. Lett.* **2014**, *408*, 155–162. [[CrossRef](#)]
87. Chu, T.; Chi, T. *Properties of Selected Ferrous Alloying Elements*; McGraw-Hill: New York, NY, USA, 1981; Volume III-1.
88. Gomi, H.; Hirose, K. Electrical resistivity and thermal conductivity of hcp Fe-Ni alloys under high pressure: Implications for thermal convection in the Earth's core. *Phys. Earth Planet. Inter.* **2015**, *247*, 2–10. [[CrossRef](#)]
89. Ezenwa, I.C.; Yoshino, T. Martian core heat flux: Electrical resistivity and thermal conductivity of liquid Fe at martian core P-T conditions. *Icarus* **2021**, *360*, 114367. [[CrossRef](#)]
90. Swartzendruber, L.J. The Fe (Iron) system. *Bull. Alloy Phase Diagr.* **1982**, *3*, 161–165. [[CrossRef](#)]

**Disclaimer/Publisher's Note:** The statements, opinions and data contained in all publications are solely those of the individual author(s) and contributor(s) and not of MDPI and/or the editor(s). MDPI and/or the editor(s) disclaim responsibility for any injury to people or property resulting from any ideas, methods, instructions or products referred to in the content.